García Villalba, M.; Palau-Salvador, G.; Rodi, W. (2014). Forced Convection Heat Transfer from a Finite-Height Cylinder. Flow, Turbulence and Combustion. 93(1):171-187. doi:10.1007/s10494-014-9543-7.

Noname manuscript No.
(will be inserted by the editor)

Forced convection heat transfer from a finite-height cylinder

Manuel García-Villalba · Guillermo Palau-Salvador · Wolfgang Rodi

Received: date / Accepted: date

Abstract This paper presents a large eddy simulation of forced convection heat transfer in the flow around a surface-mounted finite-height circular cylinder. The study was carried out for a cylinder with height-to-diameter ratio of 2.5, a Reynolds number based on the cylinder diameter of 44 000 and a Prandtl number of 1. Only the surface of the cylinder is heated while the bottom wall and the inflow are kept at a lower fixed temperature. The approach flow boundary layer had a thickness of about 10% of the cylinder height. Local and averaged heat transfer coefficients are presented. The heat transfer coefficient is strongly affected by the free-end of the cylinder. As a result of the flow over the top being downwashed behind the cylinder, a vortex-shedding process does not occur in the upper part, leading to a lower value of the local heat transfer coefficient in that region. In the lower region, vortex-shedding takes place leading to higher values of the local heat transfer coefficient. The circumferentially averaged heat transfer coefficient is 20% higher near the ground than near the top of the cylinder. The spreading and dilution of the mean temperature field in the wake of the cylinder are also discussed.

Keywords Large-eddy simulation · heat transfer · forced convection · finite-height cylinder

Manuel García-Villalba
Bioingeniería e Ing. Aeroespacial
Univ. Carlos III de Madrid, Leganés, Spain
E-mail: manuel.garcia-villalba@uc3m.es

Guillermo Palau-Salvador
Dept. Rural Engineering
Univ. Politécnica de Valencia, Valencia, Spain

Wolfgang Rodi
Inst. Hydromechanics
Karlsruhe Inst. of Technology,Karlsruhe, Germany
and
King Abdulaziz University, Jeddah, Saudi Arabia

1 Introduction

Heat transfer in the flow past obstacles plays an important role in various engineering fields. It is of particular importance in areas like energy conversion systems and for the cooling design of electric or electronic devices. The circular cylinder in crossflow is an often encountered heat transfer configuration and early studies determined experimentally the overall convective heat transfer [37,19]. Cylinders in cross-flow, especially in arrays, are used in plate-fin-tube heat exchangers which are widely used in the air conditioning and automotive industries as well as for cooling in turbomachinery [2,1]. An important region for heat transfer is the junction between the cylinder and the plate at which it is attached, where the heat-transfer characteristics are influenced by the horse-shoe vortex formed in that region [30,14,35,4]. There are many other applications in which the cylinder has a free end like for example cooling towers, oil storage tanks and electrical equipment.The structure of the flow changes near the free end and therefore the heat transfer characteristics also differ. This configuration has been studied experimentally for short cylinders by Tsutsui and co-workers [33,34] and was recently reviewed in [32]. Using oil-flow patterns and heat transfer measurements they showed the existence of several zones on top of the cylinder with different heat transfer levels: a small separation bubble near the leading edge, embedded in a large separation region with reverse flow followed by re-attached flow near the trailing edge.

In this paper we report on a Larger-Eddy Simulation (LES) of the forced convection heat transfer from a finite-height cylinder. This flow is very rich in having a variety of phenomena: it is three-dimensional, highly unsteady, and there are several interacting systems of vortices. The much studied flow past infinite cylinders is already quite complex due to the highly unsteady vortex shedding; in the case of finite-height cylinders there are in addition end effects, both on the ground side and also on the free end and these complicate further the flow and interact with the vortex shedding. For such flows, the LES technique is particularly suited because it resolves directly the unsteady shedding motions and also the larger-scale turbulent fluctuations. There are many previous works with LES applied to the flow around finite-height cylinders. For a review see [22]. More recent studies not covered in that review are the experiments of Rostamy et al. [27] or the numerical studies of Frederich and Thiele [8] and Krajnovic [17]. A very recent review concentrating on the flow over the free end is given by Sumner [32]. To the knowledge of the authors there are no LES of heat transfer from finite-height circular cylinders. Somewhat related to the present study are LES of heat transfer for other geometrical configurations, such as in pin-fin flow ([5] - albeit here the endwall was heated and not the cylindrical pins) and in flow around heated cubes [20,25], which also represent finite-height obstacles.

The configuration of the present study corresponds to one of the cases investigated by Palau-Salvador et al. [22] using experiments and large eddy simulations. These authors studied the flow around cylinders of different h/D ratios (where h is the height and D the diameter of the cylinder) at Reynolds

numbers based on the free-stream velocity and the cylinder diameter between 20000-50000. An LES of the h/D=2.5 case was earlier reported by Fröhlich and Rodi [10]. For the same configuration mass transfer from point sources close to the cylinder was studied experimentally by Donnert et al. [7] and numerically by Palau-Salvador et al. [21].

The present article is structured as follows. In §2 the setup of the simulations is described together with a brief discussion of the numerical method. In §3 the results are presented. After a description of the flow structure in §3.1, the local and average heat transfer from the cylinder are discussed in §3.2. This is followed by the study of the mean and root-mean-square (rms) temperature distribution in §3.3. Finally, conclusions are given in §4.

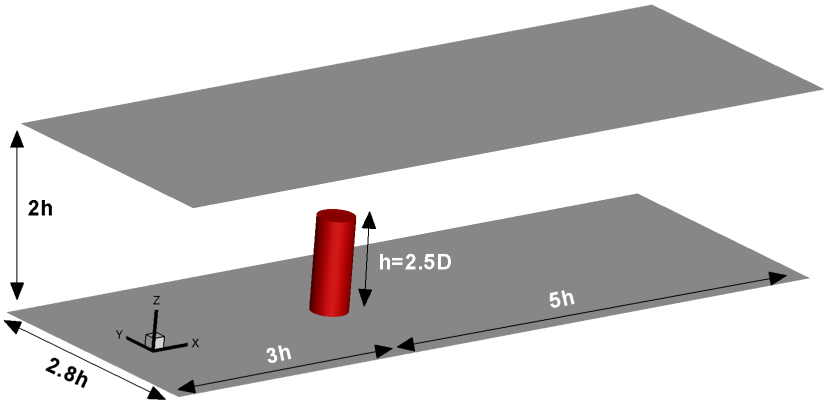

Fig. 1 Computational domain.

2 Numerical model

The LES was performed with the in-house code LESOCC2 (Large Eddy Simulation On Curvilinear Coordinates), which is the successor of the code LESOCC developed by Breuer and Rodi[3] and is described by Hinterberger [15]. The code solves the filtered Navier-Stokes equations and the filtered scalar transport equation for temperature on body-fitted, curvilinear grids using a cell-centered Finite Volume method with collocated storage for the cartesian velocity components. Second order central differences are employed for all diffusive terms and for convection terms in the momentum equations. For the temperature convection, in order to avoid overshoots and undershoots, the monotonous HLPA scheme [36] is used. The time integration is performed with a predictor-corrector scheme, where the explicit predictor step for the momentum equations is a low-storage 3-step Runge-Kutta method. The corrector step covers

the implicit solution of the Poisson equation for the pressure correction (SIMPLE). The Rhie and Chow momentum interpolation [26] is applied to avoid pressure-velocity decoupling. The Poisson equation for the pressure increment is solved iteratively by means of the 'strongly implicit procedure' of Stone [31]. Parallelization is implemented via domain decomposition, and explicit message passing is used with two halo cells along the inter-domain boundaries for intermediate storage.

The subgrid-scale (SGS) stresses in the momentum equations, resulting from the unresolved motions, are modelled using the dynamic Smagorinsky subgrid-scale model, first proposed by Germano et al.[13] and subsequently modified by Lilly [18]. In the dynamic procedure, the model parameter is determined using an explicit box filter of width equal to twice the mesh size and is smoothed by means of temporal under-relaxation [3]. Furthermore, the subgrid-scale viscosity was clipped to avoid negative values. The subgrid-scale heat fluxes in the temperature equation are determined with an eddy diffusivity model. The eddy diffusivity is related to the eddy viscosity from the dynamic Smagorinsky model with a turbulent Prandtl number of 0.6. The same numerical scheme and subgrid-scale model have been used in previous scalar transport investigations for other flows [9,6,21]. For the molecular Prandtl number a value of 1 was used in order to have the same grid resolution near walls for the velocity and temperature fields.

The configuration studied consists of the flow around a cylinder with height-to-diameter ratio h/D of 2.5 and a Reynolds number based on D and the free-stream velocity U of 44 000. The geometry of the computational domain is shown in Fig. 1. The size of the domain is $7.5h \times 2h \times 2.8h$ in streamwise, wall-normal and spanwise directions, respectively. The cross-section corresponds to the one used in the experiments [22] against which the flow calculations were validated. The body-fitted grid consists of about 50 million cells in total; it is the same as the one used by Palau-Salvador et al. [21] and is shown in two cuts in Fig. 2. The region near the cylinder is well resolved. The centre of the first cell is located at a distance $y^+ < 0.7$ from the cylinder side surface. The superscript + denotes wall units which are defined using the local friction velocity. The maximum value ($y^+ \simeq 0.7$) occurs in the region of highest speed, at about $\theta \simeq 60 - 65^\circ$ from the stagnation line. The vertical cell spacing is given by $\Delta z^+ \simeq 1.5$ and the circumferential grid spacing by $R\Delta\theta^+ \simeq 2.2$. Away from the cylinder the grid is stretched, as shown in Fig. 2. The stretching factor is 3%. Note that in the previous study [22] a different numerical method was employed, namely, a cartesian staggered grid was used and the presence of the cylinder was modelled using an immersed boundary method.

The inflow conditions were obtained by performing simultaneously a separate periodic LES of channel flow in which the mean velocity was forced to assume the experimental boundary-layer profile using a body-force technique [24]. Data from this precursor simulation were then fed in at the inflow plane. In the experiments the velocity profile was measured in the water-tunnel without cylinder. The thickness of the boundary layer was $0.1h$. This inflow-generation

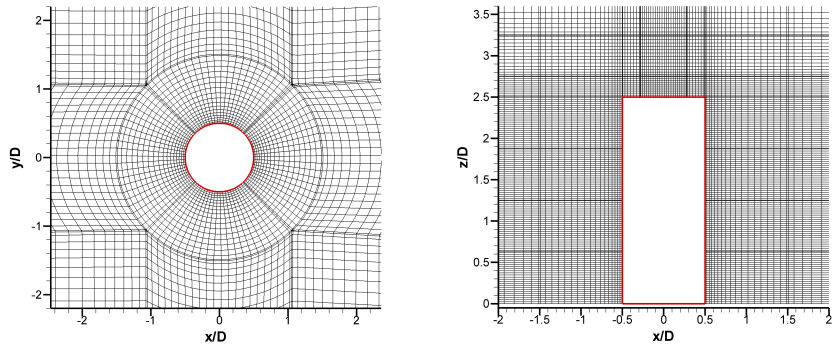

Fig. 2 Two-dimensional cuts of the grid. Every 4th grid line is shown. Left, wall-parallel plane. Right, symmetry plane.

method has been succesfully used for other flows [11,12]. A no-slip condition was employed at the bottom boundary and the cylinder surface. Free-slip conditions were used at the lateral and top boundaries and convective conditions for all quantities at the exit boundary. At the surface of the cylinder (T_1) and at the bottom wall and inlet plane (T_0), Dirichlet conditions were imposed. The temperature can be expressed as $\theta = (T - T_0)/(T_1 - T_0)$, so that at the cylinder $\theta = 1$ and at the bottom wall and inflow plane $\theta = 0$. The actual values of the temperatures T_0 and T_1 are irrelevant since the momentum and temperature equations are decoupled as the temperature is treated as a passive scalar. Homogeneous Neumann conditions were imposed for the temperature at the remaining boundaries.

A time-step $\Delta t = 0.001D/U$ was employed in the calculation. After discarding initial transients, averages were collected over 400 time units (D/U). This is a similar period as the one used in previous investigations [22] so that first and second order statistics are well converged.

3 Results

3.1 Flow description

The flow field from a previous simulation with exactly the same mesh and flow conditions as the present one was validated against experimental data in Palau-Salvador et al. [21]. Therefore, this validation is not repeated here. In that reference, the flow field was discussed in some detail, following the more extensive discussion in a previous study carried out by two of the present authors [22]. However, as the flow characteristics are very important for the heat transfer analysis, they are discussed here briefly by summarizing the overview, results and conclusions given in [22] whereby a certain repetition of the discussion in [21] is unavoidable.

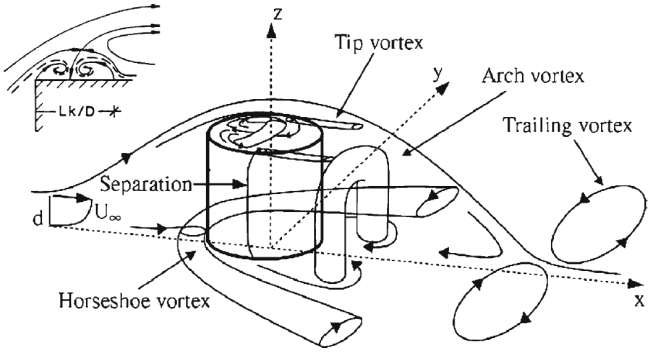

Fig. 3 Sketch of flow configuration, from Pattenden et al.[23]. Upper left insert: flow near leading edge on free end according to Hölscher and Niemann [16]

The sketch provided by Pattenden et al. [23] and reproduced in Fig. 3 gives a good overall impression of the flow around a finite-height cylinder.

This is supported by a visualization of the time-averaged flow field resulting from the present LES in Fig. 4. The figure displays in 2 oblique views the streamlines near the bottom wall, on the cylinder side and top walls and in the vertical symmetry plane of the computational domain. The streamlines on the cylinder walls are also shown in Fig. 9 below for different views corresponding to those for the heat transfer (Nu) distribution (Fig. 8).

Both Figs. 3 and 4 show that the approach flow above the usually thin boundary layer on the ground plate is deflected upwards and then over the top because the stagnation pressure in front of the cylinder is higher than the outside pressure above the free-end. In the region of the bottom boundary layer the flow is deflected downwards, and here the well-known horseshoe vortex forms which then wraps around the cylinder and extends with its two legs to the sides of the wake, interacting with this to some extent. The flow deflected over the top separates at the front edge of the cylinder and reattaches on the top surface towards the trailing edge. A complex flow develops over the free end that depends fairly strongly on the turbulent boundary layer of the approach flow.

The streamlines on the cylinder walls (Figs. 4 and 9) are rather similar to the ones reported by Palau-Salvador et al. [22], with the exception of the shape of the streamlines on the top surface. An owl-face behaviour was reported in [22] which is not reproduced here, probably due to the somewhat lower vertical resolution employed in the present study in that region, which is also responsible for a somewhat earlier reattachment. Another small difference is found on the upper rear part of the cylinder vertical wall when looking from behind. Here, the streamlines go upwards and spread sideways, while the pattern is less clear in the data of Palau-Salvador et al. [22]. Further upstream the flow separates on the side wall of the cylinder at an angle α of around 90° measured from the front stagnation line. The separation line is parallel to the

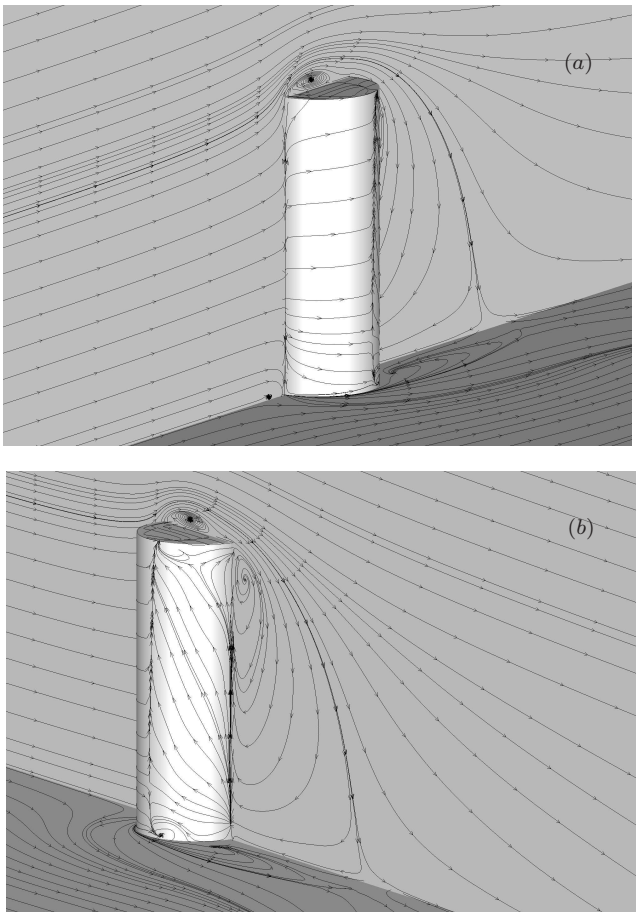

Fig. 4 Visualization of the time-averaged flow. Streamlines near the bottom-wall of the computational domain, on the symmetry plane and also near the surface of the cylinder. (*a*) Oblique view from front. (*b*) Oblique view from behind.

cylinder axis over most of the span, but is bent to the rear near the bottom and top. Behind the cylinder a wake forms, which for larger h/D ratios behaves in the main part like the vortex-shedding flow past long cylinders. However, for smaller aspect ratios the end effects are considerable. In particular, due to the lower pressure behind the cylinder, the flow over the top experiences a downwash in this region, and this flow eventually impinges on the ground plate, as can be seen in Fig. 4.

The upwash flow near the rear wall of the cylinder separates at the edge of the cylinder top forming a tip vortex that springs off this edge, similar to the one found on a delta wing. The sense of rotation is such that the flow is downwards in the centre region and upwards on the outside. The down flow in the centre region is in line with the downwash behind the cylinder. The

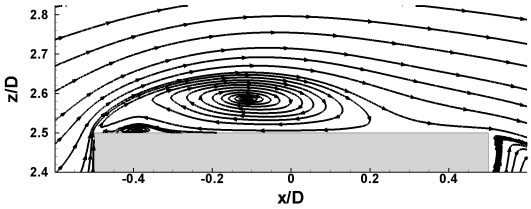

Fig. 5 Streamlines of the mean flow in the centre plane $y/D = 0$ in the cylinder top region.

tip vortices turn downwards (which is not correctly portrayed in the sketch reproduced from [23] in Fig.3), following more or less the border of the separation region, and they widen, decay and interact with the vortices shed from the sides, partly combine and merge with these until they hit the ground where they are turned in the downstream direction. They then merge with the secondary motion generated by the downwash flow hitting the ground and moving outwards in its vicinity, while higher up an inward flow exists with entrainment into the wake. The tip vortices also merge with the legs of the horseshoe vortex, which have the same sense of rotation, and finally end up in fairly large trailing vortices as sketched in Fig.3.

Under the present flow conditions, the recirculation region in the wake of the cylinder extends upto the re-attachment point at $x/D \approx 3$ (see Fig. 4 above and Fig. 4 of Ref. [21]). The horse-shoe vortex is very shallow, near the cylinder it is observed only up to $z/D \approx 0.2$ (see Fig. 4 and Fig. 10 of Ref. [21]). On top of the cylinder, the flow separates at the leading edge and re-attaches roughly at $x/D \approx 0.2$. This is shown in Fig. 5, which displays a zoom view of the streamlines of the mean flow in the symmetry plane near the top surface of the cylinder. Two recirculation bubbles are visible, the main one up to $x/D \sim 0.2$ and an embedded secondary one, quite shallow, near the edge of the cylinder in the range $-0.5 < x/D < -0.2$. The presence of these two recirculation zones and the presence of the impinging flow at reattachment will have consequences for the local heat transfer on the top surface of the cylinder as discussed in the following section. The findings are similar to those observed by Tsutsui and Kawahara [34] in their experiments (but note that in their flow schematic 4c the secondary bubble is incorrectly sketched side-by-side to the primary bubble, which is called reverse-flow region).

Figures 6 and 7 show, for various planes, the instantaneous temperature distribution at a particular instant illustrating the unsteady flow behaviour. The corresponding time-averaged temperature distributions are also shown for comparison and will be discussed below. Three horizontal planes are shown in Fig. 6 and four vertical cross-sections behind the cylinder in Fig. 7. These plots illustrate the presence of vortex-shedding past the lower part of the cylinder (below $z/D \approx 1.25$ corresponding to $z/h \approx 0.5$), while in the upper part shedding is suppressed by the free-end effect, as described above. As a consequence, the temperature field experiences much more lateral spreading near the bot-

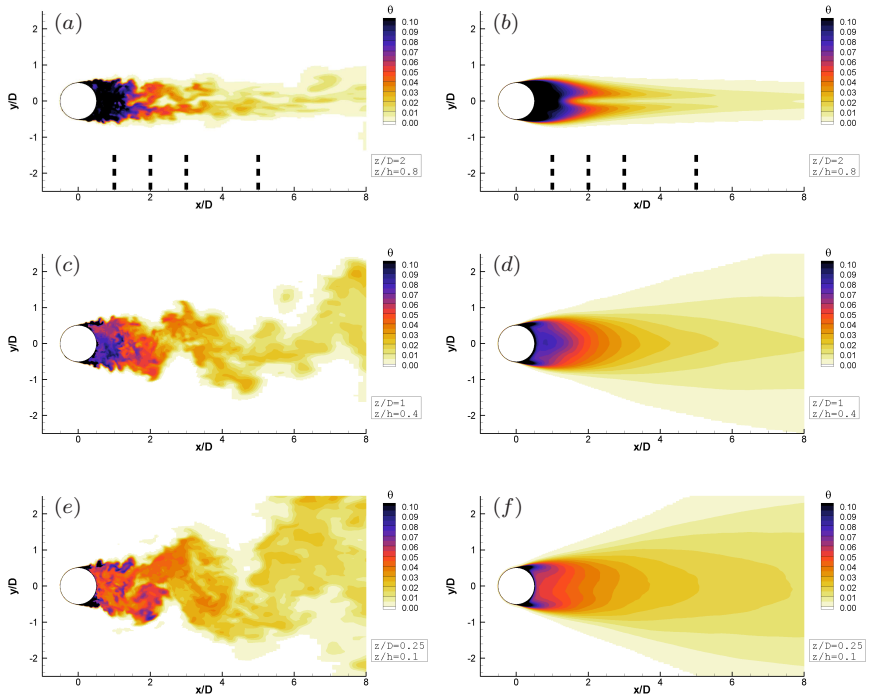

Fig. 6 Contours of instantaneous (a, c, e) and time-averaged (b, d, f) temperature distribution in three horizontal planes. The dashed lines in the top panels indicate the position of the planes shown in Fig. 7.

tom than near the cylinder top and, with growing distance from the cylinder, becomes instantaneously asymmetric near the bottom. The lateral fluctuations related with the shedding also cause stronger dilution so that near the cylinder higher temperature values are observed in the top region compared with the bottom region. This is clearly visible comparing the horizontal planes in Fig. 6 and also from the cross-section $x/D = 1$ in Fig. 7*a*. Further downstream due to the downwash effect and the evening out through fluctuations, the differences in vertical direction are much reduced.

3.2 Local and average heat transfer

In this section we discuss the Nusselt number on the cylinder walls. The Nusselt number is defined as $Nu = hD/\kappa$, where κ is the heat diffusivity of the fluid and h is the local convective heat transfer

$$h = \frac{\kappa \partial \langle T \rangle / \partial n}{T_1 - T_0} = \kappa \frac{\partial \langle \theta \rangle}{\partial n}, \tag{1}$$

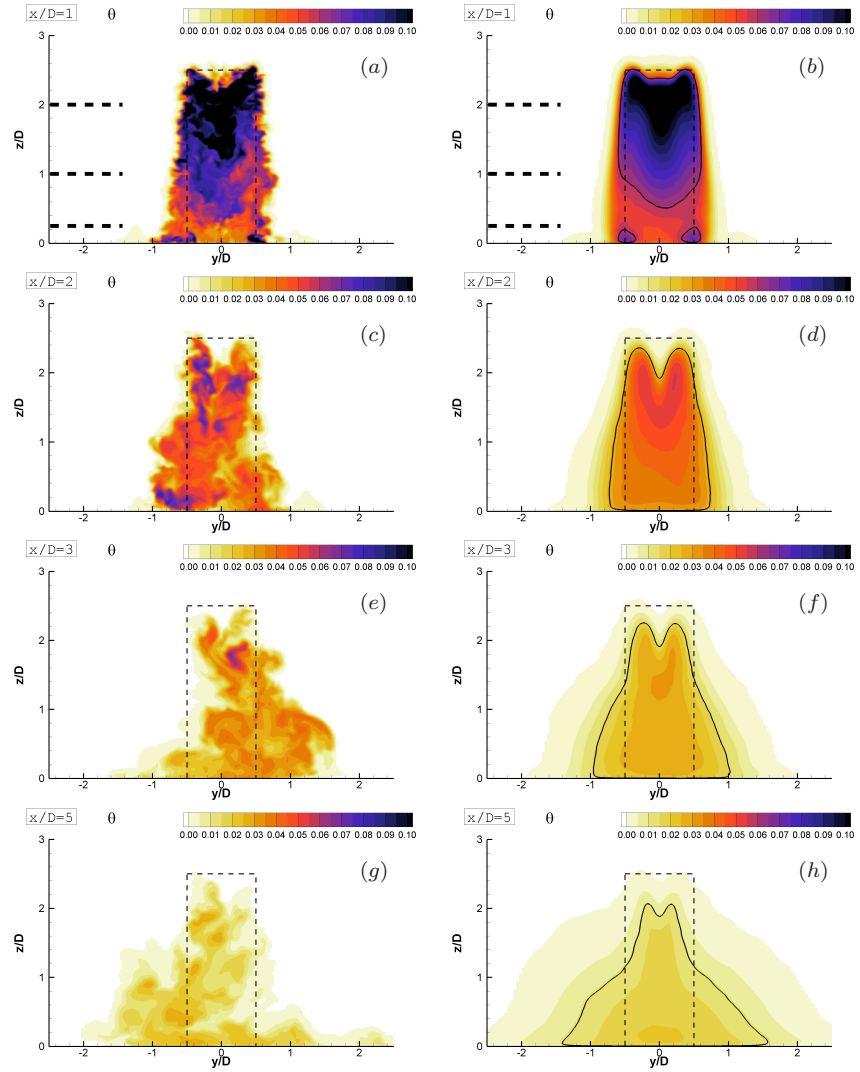

Fig. 7 Contours of instantaneous (a, c, e, g) and time-averaged (b, d, f, h) temperature distribution in four cross-sections behind the cylinder. In all panels the thin dashed line indicates the location of the cylinder. The thick dashed lines in the top panels indicate the position of the planes shown in Fig. 6.

and n denotes the normal direction to the surface. This leads to $Nu = D\partial\langle\theta\rangle/\partial n$. The local Nusselt number contours on the top and circumferential surfaces of the cylinder are shown in Fig. 8. For the circumferential surface two views are presented, a side view (from the $y-$axis) and a back view (from the $x-$axis). The streamlines of the mean flow on the cylinder walls for the same views are shown directly underneath in Fig. 9 to help with the interpretation of the

results. The contours in Fig. 8 are complemented in Fig. 10 by profiles of the local Nusselt number as a function of the angle α measured from the front stagnation line at various heights.

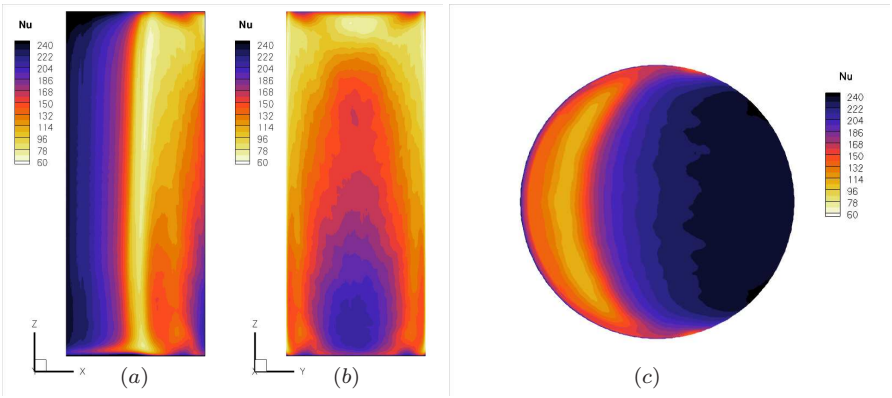

Fig. 8 Local Nusselt number. *a*) Side view. *b*) View from behind. *c*) Top view.

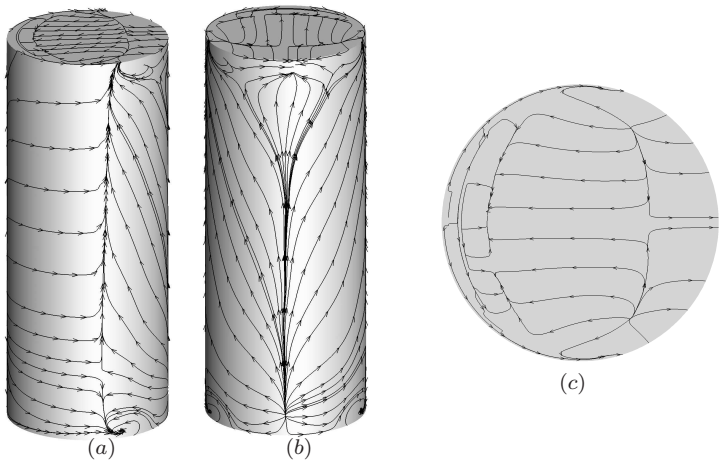

Fig. 9 Streamlines of the mean flow on cylinder walls. *a*) Side view. *b*) View from behind. *c*) Top view.

The distribution of the local Nusselt number is rather uniform over the height in the front part with the exception of the region very near the bottom and very near the top of the cylinder where ground and free-end effects play a significant role. In the front stagnation part the highest values of the local Nusselt number are reached ($Nu \approx 240$). From the side view in Fig. 8 and the

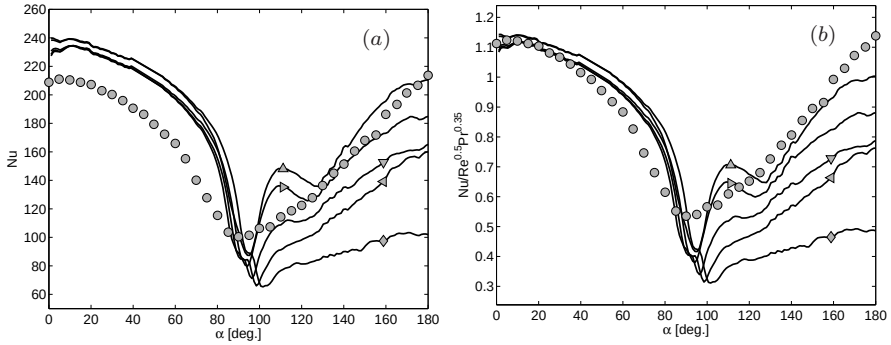

Fig. 10 *a*)Local Nusselt number as a function of the angle measured from the front stagnation line at various heights. *b*) Local Nusselt number Nu divided by $Re^{0.5}Pr^{0.35}$. — △—, $z/h = 0.1$. — ▷—, $z/h = 0.3$. — ▽—, $z/h = 0.5$. — ◁—, $z/h = 0.7$. — ◇—, $z/h = 0.9$. ○, local Nusselt number of flow over a cylinder in cross-flow (without free-end) at $Re = 44800$ and $Pr = 0.71$, experimental data [28] .

profiles in Fig. 10(a), we observe that the Nusselt number decreases with the angular position, mildly at first until $\alpha \approx 60°$. Then, the decrease is steeper in the region where the boundary layer on the cylinder separates and the minimum values are reached ($Nu \approx 60$) in a region beyond the separation line, at an angle α of about $90 - 100°$.

Up to this point the characteristics of the local Nusselt number are fairly similar at all heights as mentioned above. More interesting are the contours as seen from behind (Fig. 8b). The Nusselt number generally rises again towards the rear stagnation line, but clear differences are observed between the lower and upper regions. The values are highest near the bottom wall ($z/h = 0.1$) and decrease monotonically upwards, as can be also observed by inspection of the profiles in Fig. 10(a) for $\alpha > 100°$. The increase in Nu in the rear stagnation region is caused by the impingement of reverse flow which is stronger in the near-bottom region (see Fig. 4) and also carries lower temperature fluid (see Fig. 7a), causing higher temperature gradients at the cylinder wall. Very near the bottom of the cylinder at both sides, as seen from behind, two spots of high local Nusselt number are observed. These spots are connected with the vortex spinning off the near-bottom side wall of the cylinder seen in Fig. 4 and in the side view in Fig. 9. As discussed in [22], this vortex is likely due to the reverse flow interacting with the horse-show vortex. At the other end of the cylinder, very near the top, also towards the sides as seen from behind, there are two regions of high local Nusselt number. These two regions are likely the footprint of the tip vortices described in §3.1 and sketched in Fig. 3.

Turning now our attention to the local Nusselt number on top of the cylinder (Fig. 8c), low Nu values are observed in the front part, particularly in the region of the secondary recirculation bubble, and higher values occur towards the rear part beyond re-attachment, where the separated flow impinges on the top surface. The values of the local Nusselt number in this rear part

are comparable to the highest values reached in the front stagnation line of the cylinder. Tsutsui and Kawahara [34] measured the local Nusselt number in a similar configuration, but for shorter cylinders (upto $h/D = 1$) and with significantly higher Reynolds number and thicker incoming boundary layer. The values of the local Nusselt number are, therefore, not directly comparable. However, the shape of the contours and the streamwise distribution of the local Nusselt number on the top surface are similar to the ones here obtained (see their figure $7(a)$ - see also Fig. 19 in the review article [32]). Further, Tsutsui and Kawahara [34] provide, for a similar Reynolds number, top and side surface-average values for Nu which will be compared with the present values below.

In addition to circumferential profiles from the present study, Fig. $10(a)$ shows experimental data for heat transfer from a long cylinder in cross-flow, a statistically 2D configuration without free ends, as reported by Sanitjai and Goldstein [28]. These authors performed experiments for various Re and Pr and obtained correlations for the local Nusselt number, $Nu = f(Re, Pr)$, depending on the region of the flow around the cylinder, in their terminology: laminar boundary layer region, separation, re-attachment of shear layer (which in the mean is questionable) region and periodic vortex flow region. Here the data from their experiment with $Re = 44800$ and $Pr = 0.71$ is included in the figure. The Reynolds number in their experiment is very close to the present one, however the Prandtl number is somewhat lower, so that in the front laminar boundary layer part Nu is lower. In a companion paper Sanitjai and Goldstein [29] observed a good collapse of their data in the front part using the law $Nu \propto Re^{0.5}Pr^{0.35}$. In figure $10(b)$ the quantity $Nu/Re^{0.5}Pr^{0.35}$ is displayed. Indeed, good agreement between the experimental and computed values can now be observed in the front region before separation. In the rear part, the turbulent recirculation region is dominant, and Pr appears to play no major role there. Sanitjai and Goldstein [29] did not observe a variation of Nu in that region when changing Pr. In the rear part, it is noteworthy that the Nusselt number from the present calculation in the lower part of the cylinder ($z/h \leq 0.3$) reaches similar values as the Nusselt number in the experiments (Fig. $10a$). In that region the flow is governed by vortex shedding, as discussed above. Vortex shedding is also dominant in the 2D configuration of Sanitjai and Goldstein [28] which explains the agreement. In this region the Nu distribution has a hump around $\alpha \approx 110°$, and such hump behaviour was also observed by Sanitjai and Goldstein [28] in their experiments. This hump behaviour is likely to be caused by the intermittent impingement of shed vortices on the rear of the cylinder, as can be seen in the animations presented in [7]. Further upwards where the flow is subject to free-end effects no vortex shedding is observed and the values of the Nusselt number are lower.

The circumferentially averaged heat transfer coefficient is calculated by averaging over the circumferential direction at each height. The resulting averaged Nusselt number is displayed in Fig. 11 as a function of z/h. The maximum value of the averaged Nusselt number is reached at $z/h \approx 0.1$, $\overline{Nu}_{max} \sim 185$. As expected from the contours of the local Nusselt number, the averaged Nus-

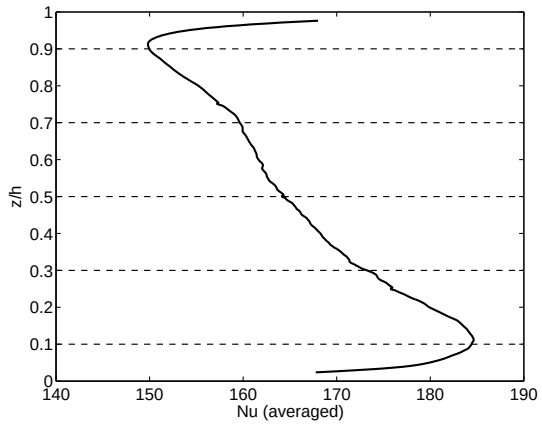

Fig. 11 Circumferentially-averaged Nusselt number as a function of z/h. The dashed lines indicate the height at which profiles are shown in Fig. 10.

selt number decreases with increasing height above the bottom. The minimum value occurs near $z/h = 0.9$, $\overline{Nu}_{min} \sim 150$. The presence of the ground wall results in a decrease (from the maximum value) of the averaged Nusselt number, while reaching the free-end results in an increase (from the minimum value). For reference, the value of the averaged Nusselt number in the case of a long cylinder in cross-flow can be obtained from an empirical correlation (eq. (19) of Sanitjai and Goldstein [28]), using $Re = 44000$ and $Pr = 1$ an average Nusselt number of 178.4 is obtained. The maximum value obtained in the present study is 3,7% larger than this reference value and the minimum value is 16% lower. It can be concluded that the downwash flow from the top that limits the vortex-shedding process in the upper region of the cylinder leads to a reduced value of the heat transfer coefficient.

Averages of the Nusselt number over the entire side surface ($\overline{Nu}_s$) and top surface ($\overline{Nu}_t$) were also calculated to yield $\overline{Nu}_s = 166.6$ and $\overline{Nu}_t = 195.8$. Although the experiments of Tsutsui & Kawahara [34] correspond to much lower h/D ratios, we have extracted manually from their Fig. 9 the data for the case $h/D = 1$ and $Re \simeq 42000$ ($D = 80$ mm). The values extracted are $\overline{Nu}_s \simeq 186$ and $\overline{Nu}_t \simeq 210$. The calculated values for $h/D = 2.5$ are somewhat lower than the measured ones for $h/D = 1$, which is consistent with the trend in their Fig. 10 showing that $\overline{Nu}_s$ and $\overline{Nu}_t$ decrease with increasing h/D. Hence, there is reasonable support of the calculated values by the experiments of [34], also concerning the finding that the Nusselt number on the top surface is higher than that on the side surface.

3.3 Mean and rms temperature distribution

In this section we concentrate on the mean and rms temperature distribution in the wake of the cylinder, $\langle\theta\rangle$ and θ^{rms}, respectively. Fig. 6 shows contours of the time-averaged temperature distribution at three horizontal planes and Fig. 7 at four cross-sections in the wake of the cylinder at $x/D = 1$, 2, 3 and 5. Near the cylinder, at $x/D = 1$, the highest values of the temperature are observed near the top of the cylinder, and the temperature decreases downwards, reflecting the fact that the lateral mixing with colder ambient fluid is more effective in the lower part. Further downstream, we observe that the region of maximum temperature is displaced towards the bottom wall, as a result of the downwash bringing the heated fluid from the near-top region to this wall. As can be seen clearly in Figs. 6 and 7, the lateral spreading of the temperature plume is considerably more pronounced in the lower part of the cylinder, as a result of the vortex shedding present in that region. In fact, at the level near the top (Fig. 6*b*) the plume actually reduces somewhat in width due to the downward movement of heated fluid and the inward movement of ambient fluid by the evolving secondary motion (see Fig. 19 in [22]).

The evolution of $\langle\theta\rangle_{max}$, the maximum mean temperature $\langle\theta\rangle_{max}$ of each cross-section, with streamwise direction is shown in Fig. 12(a) in semi-logarithmic scale. The maximum temperature decreases very steeply very near the cylinder, in a distance roughly of $0.1D$ it decreases from the value at the wall $\langle\theta\rangle_{max} = 1$ to $\langle\theta\rangle_{max} \approx 0.2$. With increasing x, $\langle\theta\rangle_{max}$ decreases quickly up to the bottom re-attachment point $x/D \approx 3$. Beyond re-attachment the streamwise decay of $\langle\theta\rangle_{max}$ happens at a lower rate, because the trailing vortices in that region are weak leading to a lower mixing rate. A similar observation was made for the dilution of tracers in this configuration[21].

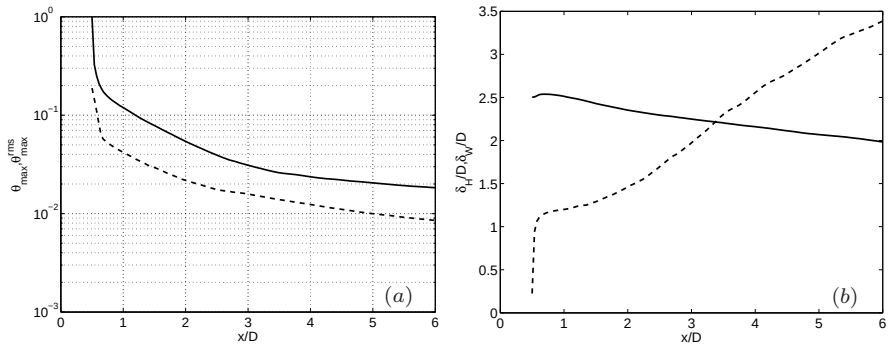

Fig. 12 *a*) Maximum mean temperature $\langle\theta\rangle_{max}$ (solid line) and maximum rms temperature fluctuations θ^{rms}_{max} (dashed line) in each cross-section as a function of x/D. *b*) Height δ_H/D (solid line) and width δ_W/D (dashed line) of the temperature plume as a function of x/D.

We try now to quantify the spreading of the temperature plume. To this end we define the height δ_H and the width δ_W of the temperature plume using at each cross-section the contour where $\langle\theta\rangle$ is half the maximum value. Such contours are shown in Fig. 7 with a thick line. The height of the temperature plume δ_H is defined at each cross-section as z_{max} of the $0.5\langle\theta\rangle_{max}$ contour line. Similarly, the width of the temperature plume is defined as $2y_{max}$ (the factor 2 is added to obtain the full width) of the $0.5\langle\theta\rangle_{max}$ contour line. Both quantities are displayed as a function of x/D in Fig. 12(b). The width of the plume grows as a result of the vortex shedding process. The height of the plume decreases as a result of the downwash flow from the top of the cylinder. However the rate of decrease of the height δ_H is much slower than the rate of growth of the width δ_W.

Fig. 13 shows contours of the rms values of the temperature fluctuations at four cross-sections in the wake of the cylinder at $x/D = 1$, 2, 3 and 5. The evolution of θ^{rms}_{max} as a function of x/D is shown in Fig. 12 and follows a similar trend as the maximum mean temperature. Near the cylinder, at $x/D = 1$, the rms values are concentrated in the shear layer that is formed at the boundary between the free-stream and the recirculation zone behind the cylinder. Lower values are observed within the recirculation zone and negligible ones in the outside region. Interestingly, the highest values occur near $y = 0.5D$ both near the ground and near the top of the cylinder. These regions are affected by the unsteadiness of the cylinder-foot (see Fig. 9) and horse-shoe vortex (bottom) and tip vortices (top). Further downstream, a similar trend as the for mean temperature distribution is observed. The region of intense turbulent activity broadens in the lower part, as a result of the vortex-shedding and the outward motion of the trailing vortex in this region, and it is displaced towards the wall. For example, relatively far from the cylinder at $x/D = 5$, maximum values of θ^{rms} occur around $y/D \approx 1.1$, $z/D \approx 0.6$. However, non- negligible values are observed in a quasi-triangular region extending upto $y/D \approx 2.5$ in the lower part and upto $z/D \approx 2.5$ in the central region.

4 Conclusions

The forced convection heat transfer from a surface-mounted finite-height circular cylinder at $Re = 44000$ and $Pr = 1$ has been studied using the results of a large eddy simulation. The flow field was validated in a previous study [21]. In absence of experimental data of heat transfer matching the present configuration, confidence on the heat transfer results from the present simulation has been obtained by comparing the heat transfer coefficient in the front part of the cylinder and also for the lower rear part with vortex-shedding to experimental data from a long cylinder in crossflow [28]. Also, the calculated averaged Nusselt numbers on the top and side surfaces of the cylinder are well supported by the measurements of Tsutsui and Kawahara [34] for a shorter finite-height cylinder.

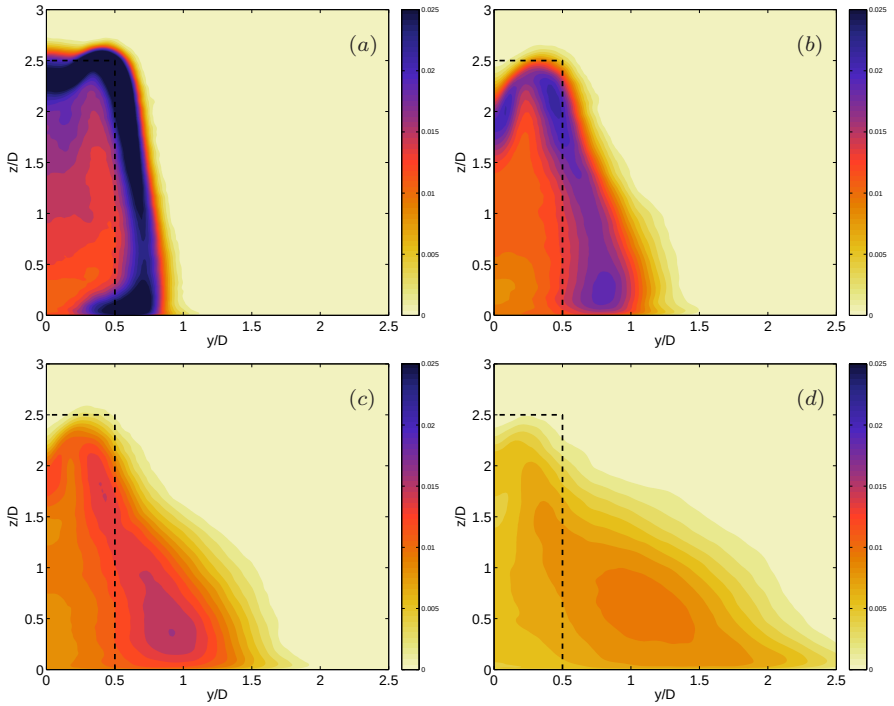

Fig. 13 Contours of rms of temperature fluctuations at cross sections x/D=1,2,3 and 5. The dashed line indicates the location of the cylinder.

It has been observed that the free-end effect has a strong influence on the heat transfer from the cylinder. Specifically, the flow coming over the top experiences a downwash behind the cylinder due to the lower pressure in this region. This suppresses the vortex shedding process in the upper region of the cylinder leading to lower values of the local Nusselt number. In contrast, in the lower part (below $z/h \approx 0.5$) vortex shedding does take place and the values of the local Nusselt number in this region are higher. When the Nusselt number is averaged circumferentially, about a 20% higher value is obtained near the bottom ($z/h = 0.1$) compared to the averaged Nusselt number near the top ($z/h = 0.9$). The effect of the horse-shoe vortex on the local Nusselt number is small for the present configuration, since it is confined to a very small region near the ground due to the small thickness of the incoming boundary layer. However, interacting with the reverse flow in the rear of the cylinder it does leave a footprint in the local Nusselt number contours near the ground. Similarly, the effect of the tip vortices is small. The contours of the local Nusselt number on the top of the cylinder present similar characteristics as the ones measured by Tsutsui and Kawahara [34]. Lower values are observed in the region affected by recirculating flow and once the flow re-attaches the

local Nusselt number reaches values as large as those occuring around the front stagnation line.

It has been also shown that the structure of the mean and rms temperature distributions in the wake of the cylinder is governed by the highly complex and three-dimensional mean flow. The distributions of both spread laterally in the lower part due to the vortex shedding process ocurring in that region, while almost no spreading is observed in the upper region.

Acknowledgements The simulation was carried out using the supercomputing facilities of the Steinbuch Centre for Computing (SCC) of the Karlsruhe Institute of Technology. MGV has been partially supported by grant TRA2012-37714 of the Spanish Ministry of Economy and Competitiveness.

References

1. Ames, F., Dvorak, L.: Turbulent transport in pin fin arrays: experimental data and predictions. J. Turbomachinery **128**(1), 71–81 (2006)
2. Armstrong, J., Winstanley, D.: A review of staggered array pin fin heat transfer for turbine cooling applications. J. Turbomachinery **110**, 94 (1988)
3. Breuer, M., Rodi, W.: Large eddy simulation of complex turbulent flows of practical interest. In: E. Hirschel (ed.) Flow simulation with high performance computers II, Notes on Numerical Fluid Mechanics, vol. 52, pp. 258–274. Vieweg, Braunschweig (1996)
4. Chen, S., Sanitjai, S., Ghosh, K., Goldstein, R.: Three-dimensional vortex flow near the endwall of a short cylinder in crossflow: Uniform-diameter circular cylinder. Appl. Thermal Eng. **49**, 73–78 (2012)
5. Delibra, G., Hanjalic, K., Borello, D., Rispoli, F.: Vortex structures and heat transfer in a wall-bounded pin matrix: LES with a RANS wall-treatment. Int. J. Heat Fluid Flow **31**(5), 740–753 (2010)
6. Denev, J.A., Fröhlich, J., Bockhorn, H.: Large eddy simulation of a swirling transverse jet into a crossflow with investigation of scalar transport. Phys. Fluids **21**, 015,101 (2009)
7. Donnert, G.D., Kappler, M., Rodi, W.: Measurement of tracer concentration in the flow around finite-height cylinders. J. Turbul. **8**, 33 (2007)
8. Frederich, O., Thiele, F.: Turbulent flow dynamics caused by a truncated cylinder. Int. J. Heat Fluid Flow **32**(3), 546–557 (2011)
9. Fröhlich, J., García-Villalba, M., Rodi, W.: Scalar mixing and large–scale coherent structures in a turbulent swirling jet. Flow Turbul. Combust. **80**, 47–59 (2008)
10. Fröhlich, J., Rodi, W.: LES of the flow around a cylinder of finite height. Int. J. Heat Fluid Flow **25**, 537–548 (2004)
11. García-Villalba, M., Fröhlich, J.: LES of a free annular swirling jet – dependence of coherent structures on a pilot jet and the level of swirl. Int. J. Heat Fluid Flow **27**(5), 911–923 (2006)
12. García-Villalba, M., Li, N., Rodi, W., Leschziner, M.A.: Large eddy simulation of separated flow over a three-dimensional axisymmetric hill. J. Fluid Mech. **627**, 55–96 (2009)
13. Germano, M., Piomelli, U., Moin, P., Cabot, W.: A dynamic subgrid-scale eddy viscosity model. Phys. Fluids **3**, 1760–1765 (1991)
14. Hinckel, J.N., Nagamatsu, H.T.: Heat transfer in the stagnation region of the junction of a circular cylinder perpendicular to a flat plate. Int. J. Heat Mass Transfer **29**(7), 999–1005 (1986)
15. Hinterberger, C.: Dreidimensionale und tiefengemittelte Large-Eddy-Simulation von Flachwasserströmungen. Ph.D. thesis, University of Karlsruhe (2004)
16. Hölscher, N., Niemann, H.J.: Some aspects about the flow around a surface-mounted circular cylinder in a turbulent shear flow. In: Proc. 6th Symp. Int. Turbulent Shear Flows, Toulouse (1987)

17. Krajnovic, S.: Flow around a tall finite cylinder explored by large eddy simulation. J. Fluid Mech. **676**, 294–317 (2011)
18. Lilly, D.: A proposed modification of the Germano subgrid-scale closure method. Phys. Fluids **4**, 633–635 (1992)
19. Morgan, V.T.: The overall convective heat transfer from smooth circular cylinders. Adv. Heat Transfer **11**, 199–264 (1975)
20. Ničeno, B., Dronkers, A., Hanjalić, K.: Turbulent heat transfer from a multi-layered wall-mounted cube matrix: a large eddy simulation. Int. J. Heat Fluid Flow **23**(2), 173–185 (2002)
21. Palau-Salvador, G., García-Villalba, M., Rodi, W.: Scalar transport from point sources in the flow around a finite-height cylinder. Environ. Fluid Mech. **11**, 611–625 (2011)
22. Palau-Salvador, G., Stoesser, T., Fröhlich, J., Kappler, M., Rodi, W.: Large-Eddy Simulations and experiments of flow around finite-height cylinders. Flow Turbul. Combust. **84**, 239–275 (2010)
23. Pattenden, R., Turnock, S., Zhang, X.: Measurements of the flow over a low-aspect ratio cylinder mounted on a ground plate. Exp. Fluids **39**, 10–21 (2005)
24. Pierce, C.: Progress-variable approach for large-eddy simulation of turbulent combustion. Ph.D. thesis, Stanford University (2001)
25. Popovac, M., Hanjalic, K.: Vortices and heat flux around a wall-mounted cube cooled simultaneously by a jet and a crossflow. Int. J. Heat Mass Transfer **52**(17-18), 4047–4062 (2009)
26. Rhie, C., Chow, W.: Numerical study of the turbulent flow past an airfoil with trailing edge separation. AIAA J. **21**(11), 1061–1068 (1983)
27. Rostamy, N., Sumner, D., Bergstrom, D.J., Bugg, J.D.: Local flow field of a surface-mounted finite circular cylinder. J. Fluids Struct. **34**, 105–122 (2012)
28. Sanitjai, S., Goldstein, R.J.: Forced convection heat transfer from a circular cylinder in crossflow to air and liquids. Int. J. Heat Mass Transfer **47**, 4795–4805 (2004)
29. Sanitjai, S., Goldstein, R.J.: Heat transfer from a circular cylinder to mixtures of water and ethylene glycol. Int. J. Heat Mass Transfer **47**, 4785–4794 (2004)
30. Sparrow, E.M., Stahl, T.J., Traub, P.: Heat transfer adjacent to the attached end of a cylinder in crossflow. Int. J. Heat Mass Transfer **27**(2), 233–242 (1984)
31. Stone, H.: Iterative solution of implicit approximations of multidimensional partial differential equations for finite difference methods. SIAM J. Numer. Anal. **5**, 530–558 (1968)
32. Sumner, D.: Flow above the free end of a surface-mounted finite-height circular cylinder: A review. J. Fluids Struct. **43**, 41–63 (2013)
33. Tsutsui, T., Igarashi, T., Nakamura, H.: Fluid flow and heat transfer around a cylindrical protuberance mounted on a flat plate boundary layer. JSME Series B **43**(2), 279–287 (2000)
34. Tsutsui, T., Kawahara, M.: Heat transfer around a cylindrical protuberance mounted in a plane turbulent boundary layer. J. Heat Transfer **128**, 153–161 (2006)
35. Tutar, M., Akkoca, A.: Numerical analysis of fluid flow and heat transfer characteristics in three-dimensional plate fin-and-tube heat exchangers. Num. Heat Transfer Part A **46**, 301–321 (2004)
36. Zhu, J.: Low diffusive and oscillation–free convection scheme. Comm. Appl. Num. Meth. **7**, 225–232 (1991)
37. Zukauskas, A.A.: Heat transfer from tubes in cross-flow. Adv. Heat Transfer **8**, 93–160 (1972)